

*This paper was recommended for publication in revised form by Regional Editor Derya Burcu Özkan*

## INVESTIGATION OF NANOFLUID FLOW CHARACTERISTICS AND WALL STRESS CONCENTRATION LOCATIONS IN A 3D CHANNEL WITH SHARP EDGE RECTANGULAR RIBS

**\*M. Murat Yavuz**

Osmaniye Korkut Ata University  
Osmaniye, Turkey

**Nehir Tokgöz**

Osmaniye Korkut Ata University  
Osmaniye, Turkey

*Keywords:* Channel flow, Stress concentrations

*\* Corresponding author:* Phone: 0(328) 825 18 18

*E-mail address:* muratyavuz@osmaniye.edu.tr

### ABSTRACT

Flow regimes in various channels can introduce different responses that interact with inside of channel walls. Hence both flow characteristic and its effect on wall surfaces should be investigated, especially for a new channel design or usage of a new fluid. In this work, flow characteristics of a nanofluid flow and wall stress concentration locations are investigated numerically in a 3D channel with including sharp edge rectangular ribs. The ribs are arranged with periodic order and transverse positions at inside of upper and below surfaces of channel. The nanofluid flow consists of  $Al_2O_3$ -water solution with %8 particle volume concentrations. The used Reynolds number (Re) changes from 75 to 2000. Furthermore, commonly used two different fluids are investigated for detecting differences of flow characteristics of nanofluid. Tresca yield criterion is used with considering channel's ductile material properties in stress analysis. Interactions between ribs and flow are observed in detail. Flow separation and vortex formations effectively depend on Reynolds number. Values of wall stress concentrations depend on Reynolds number and pressure effects with respect to sharp edge rectangular ribs. Stress values of upper surfaces are less than along path of below surfaces on channel wall surfaces.

### INTRODUCTION

The heat generates in the majority of engineering applications and it is important to transfer it to desired locations. As a result of performing the heat transfer, appropriate systems must be designed with considering effective parameters. Increment of

heat transfer surface is commonly applied for increasing heat transfer capacity. However, this condition causes to increase sizes of heat transfer systems, cost and also pressure loss with respect to included fins inside the channels. Hence, more effective heat transfer systems must be developed.

Addition of rib-groove formations inside channels can be effective in a limited range on heat transfer [1-7]. Their geometries directly influence flow behaviour and also heat transfer capacity. Different shaped ribs/grooves are studied in literature for detecting optimum shaped ribs/grooves [8-10]. Also different vortex generators/turbulators are investigated. Two review studies on solar thermal systems and usage of turbulators [11-12] point the usage of delta winglets, which generates vortices that increase heat transfer without much increase in friction factor. Vortex generators [13] are included inside of a solar air heater to increase turbulent intensity. This application [14] is applied in another solar heat study with including obstacles on an absorber plate, which supports larger flow recirculation that increases production rate of turbulent kinetic energy and heat transfer rate. Similar phenomenon is observed [15] in the investigation of z-shaped turbulator baffles on heat transfer, which causes to formation of co-rotating vortex flows, that increases the flow turbulence intensity. The usage of both ribs and turbulators [16] increases Nusselt number and friction factor more than alone usage of ribs or vortex generators. Meanwhile, the orientation of included rib turbulators [16-17] has been effective on heat transfer performance. Perforated conical-ring (PCR) [18] is one of the turbulator types, which prevents the development of thermal boundary layer and maintains an effective heat transfer in a

plain tube. However, the developed turbulent flow conditions [19-21] with increasing Re can increase pressure drop drastically and they must be also considered in the analyses. Friction factor [22] increases with addition of ribs into smooth tubes, which are used for both forced convection and mixed convection. Also, if flow separation [23] locations occur, heat transfer capacity decreases. Heat transfer enhancement is achieved in a limited range in those studies. However more studies are needed, especially for 3D cases.

Fluids are commonly used for transferring the heat from a solid surface. Fluid provides heat transfer with convection and therefore heat transfer properties of fluid are important. For this purpose, special fluids have been developed, especially usage for refrigeration systems and heat transfer applications. Also special particles are included into fluids for increasing heat transfer capacity, which are called nanofluids [24] with respect to their sizes. Different nanofluid particles are available in literature [25-26]. They can be used as mixture or two-phase flow condition. Generally heat transfer efficiency with addition of nanofluid flow depends on nanofluid particle volume concentration and commonly increases linearly [2,27]. However this phenomenon can respond nonlinear behaviour in some cases.

The findings in literature show that heat transfer efficiency depends on different parameters, as flow characteristics of fluid, geometrical shape of channel heat transfer surface, thickness and so on. They must be also considered for designing optimum heat transfer system. Fluid flow conditions in heat transfer systems are important. Prevention of flow separation must be investigated carefully with considering channel geometry.

The thickness of heat exchangers and their parts influences the performance of heat transfer. If heat exchangers and components are constructed with small thicknesses, better heat transfer performance can be achieved, especially variable temperatures in time dependent solutions. However, strength of heat exchangers and components decreases to withstand the fluid pressure and thermal stresses. Hence effect of thickness on stress formations must be investigated carefully. It is commonly known that sharp edges in a fluid flow system causes flow separations and also causes stress concentrations in mechanical strength analysis.

In this study, flow characteristics of nanofluid flow in a 3D channel is investigated with considering various Reynolds number. Wall stress concentration locations are determined. The results are compared with water and argon solution results, which are also solved in this study. A 3D channel with included ribs is constructed with respect to the study of [9]. The gained results will show how to optimize heat transfer system on flow characteristics of fluid and strength of channel.

## MATERIAL AND METHOD

Nanofluid particles can be used in mixture or two phase flow as included granule structures. In this study, nanoparticles are used within water solution as a mixture. The nanofluid flow consists of Al<sub>2</sub>O<sub>3</sub>-water solution with %8 particle volume concentrations. Addition of Al<sub>2</sub>O<sub>3</sub> nanoparticles [25-26, 28-29] are widely used in nanofluid analyses in literature and they are also used in this study.

Nanofluid solution results are compared with pure water and argon flow results. Argon properties [9] have a density ( $\rho$ ) of 1.62 kg/m<sup>3</sup>, specific heat ( $c_p$ ) of 520.64 J/kg.K, thermal conductivity ( $\lambda$ ) of 0.0158 W/m.K and dynamic viscosity ( $\mu$ ) of  $2.16 \times 10^{-5}$  kg/m.s. Initial temperature ( $T_{inlet}$ ) of argon at the inlet section is 293 K. The walls have a constant temperature of ( $T_{walls}$ ) 313 K. These temperatures are given for providing same geometry and boundary conditions of the study [9], however they have no effective on flow and strength analyses. Thermal stresses are neglected. Reynolds number (Re) is used as 75, 200, 500, 1000, 1500 and 2000. The velocity (V) of inlet flow of argon is 0.14 m/s, 0.37 m/s, 0.93 m/s, 1.86 m/s, 2.80 m/s and 3.73 m/s, which changes with respect to Re. The used Re is in a range of laminar flow zone. No transient or turbulence flow responses are considered. Its representation is given in Eq. 1.

$$Re = \frac{\rho V D_h}{\mu} \quad (1)$$

where  $D_h$  is hydraulic diameter of channel section, is equal to  $(2hw)/(h+w)$ .

Water properties have a density ( $\rho_{nano}$ ) of 998.2 kg/m<sup>3</sup>, specific heat ( $c_{p,nano}$ ) of 4066 J/kg.K, thermal conductivity ( $\lambda_{nano}$ ) of 0.63842 W/m.K and dynamic viscosity ( $\mu_{nano}$ ) of 0.0005797 kg/m.s. Fluid properties with including nanoparticles have a density ( $\rho_{nano}$ ) of 1222 kg/m<sup>3</sup>, specific heat ( $c_{p,nano}$ ) of 3257.6 J/kg.K, thermal conductivity ( $\lambda_{nano}$ ) of 0.8765 W/m.K and dynamic viscosity ( $\mu_{nano}$ ) of 0.000714 kg/m.s. All solutions are carried out with these properties and configurations. The velocity (V) of inlet flow for water and argon is 0.00627 m/s, 0.01672 m/s, 0.0418 m/s, 0.0836 m/s, 0.1254 m/s and 0.167 m/s, which changes with respect to Re.

The geometry of channel is given in Fig. 1 and detail view of one of section pattern is given in Fig. 2. Each section pattern has a length ( $l_{sm}$ ) of 17.5 mm, a height (h) of 10.5 mm and a width (w) of 5.25 mm. Totally 8 section patterns are included and a smooth rectangular channel continues. Total length of the whole analysed model is 193.9 mm. The opposite ribs have a length ( $l_r$ ) of 3.86 mm, a height ( $h_r$ ) of 3.5 mm and a width ( $w_r$ ) of 5.25 mm. Ribs have rectangular shapes and their edges are not rounded.  $x_{r,up}$  represents stress results taken path on upper

wall surface and  $x_{r,up}$  represents stress results taken path on lower wall surface.

Computational fluid dynamic analyses are used in solution cases. All models and solutions are carried on FLUENT 14.5 package software. Laminar ( $Re=75$ ) and renormalized  $k-\epsilon$

turbulence ( $Re>75$ ) models are used with considering Reynolds number and turbulences at flow solutions. The used  $k-\epsilon$  turbulence model [30] achieves the best results for 2D flow through conventional solar air

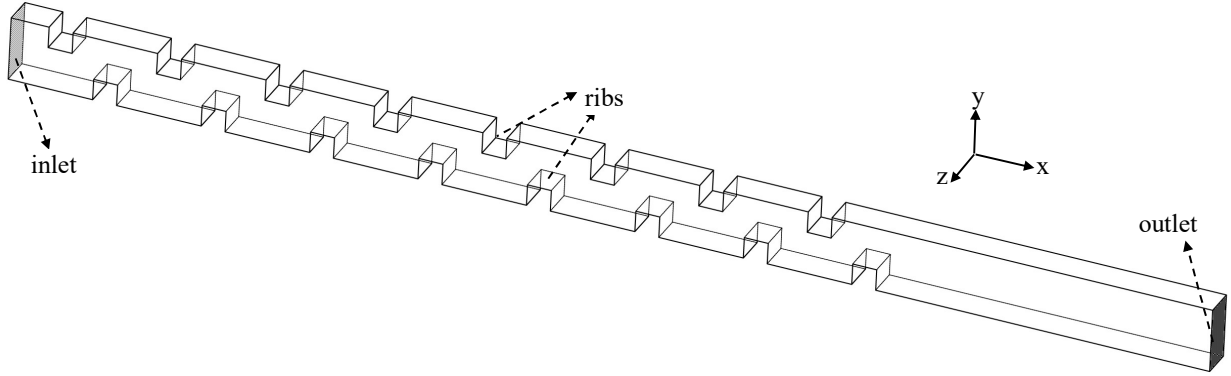


Figure 1 Geometry of channel

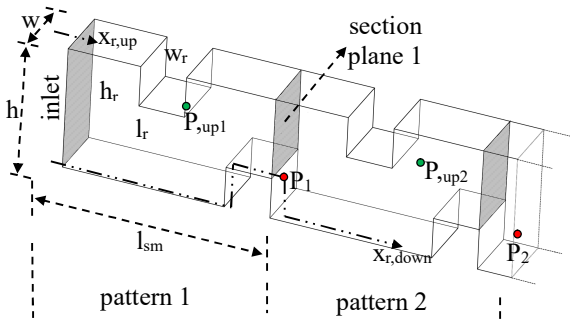


Figure 2 Closer view of patterns

heaters, which is compared with different turbulence models. The reason why  $k-\epsilon$  turbulence model is used in such  $Re$  can be explained with the compared study findings [9], which uses  $k-\epsilon$  turbulence model for prevention of periodic oscillations of equations residuals in  $Re$  solutions between 100 and 2000. The arranged ribs with periodic order and transverse positions cause oscillatory flow appearance and behaviour, which usually sustain in low  $Re$  solution of heat transfer enhancement studies, that cause convergence problems in laminar flow laws. A critical  $Re$  ( $Re_c$ ) [9] is considered for this case. Convergence criteria for continuity are selected as  $10^{-5}$  and for momentum equations are selected as  $10^{-6}$ . Default SIMPLE solver is used in solutions.

Turbulent intensity is given in Eq. 2, which effective especially on high  $Re$  solutions. The flow begins from inlet section perpendicularly and flows through the channel. Even if increasing [31] the pulsating inlet velocity for increasing total heat transfer and flow resistance in the channel, there are no oscillations occur at the inlet in this study.

$$I = 0.16Re^{-1/8} \quad (2)$$

The Fanning friction factor is given in Eq. 3 for investigation of pressure changes;

$$F_f = \frac{D_s \Delta P}{2\rho V^2 L} \quad (3)$$

The walls are made of aluminium, which is commonly used in heat exchanger materials [32-33] in literature and it has a thermal conductivity ( $\lambda_{alu}$ ) of 204 W/m.K, density ( $\rho_{alu}$ ) of 2707 kg/m<sup>3</sup> and a specific heat ( $c_{p,alu}$ ) of 896 J/kg.K. Aluminium alloy [34] 1100-H14 (99% Al) is used in strength analyses, which has yield strength of 95 MPa in tension ( $\tau_{y,tension}$ ) and 55 MPa in shear ( $\tau_{y,shear}$ ), ultimate strength of 110 MPa in tension ( $\tau_{ult,tension}$ ) and 70 MPa in shear ( $\tau_{ult,shear}$ ), Modulus of Elasticity (E) of 70 GPa and Poisson's ratio ( $\nu$ ) [35] of 0.3. The temperature of walls has constant temperature from the beginning of the solutions. Hence coefficient of thermal expansion is not necessary.

In literature, overall thicknesses of heat exchangers, which are mainly made of aluminium alloys, are vary between 0.1 mm and 1.5 mm [36-39]. The wall thickness is selected 1 mm in the analyses. Numerical model is given in Fig. 3, which has approximately 4.800.000 hexahedral grid elements.

### NUMERICAL ANALYSE CONDITIONS AND CALCULATIONS

$k-\epsilon$  RNG turbulence model [40] is used in the solutions. This solution technique includes  $k$  (kinetic energy transport) and  $\epsilon$  (dissipation) equations and they are given in Eq. 4 and 5, respectively.

$$\frac{\partial}{\partial t}(\rho k) + \frac{\partial}{\partial x_i}(\rho k u_i) = \frac{\partial}{\partial x_j} \left( \alpha_e \mu_{eff} \frac{\partial k}{\partial x_j} \right) + G_k + G_b - \rho \varepsilon - Y_M + S_k \quad (4)$$

turbulence kinetic energy with respect to mean velocity gradients and buoyancy and they are given in Eq. 6 and 7.

$$\frac{\partial}{\partial t}(\rho \varepsilon) + \frac{\partial}{\partial x_i}(\rho \varepsilon u_i) = \frac{\partial}{\partial x_j} \left( \alpha_e \mu_{eff} \frac{\partial \varepsilon}{\partial x_j} \right) + C_{1\varepsilon} \frac{\varepsilon}{k} (G_k + C_{3\varepsilon} G_b) - C_{2\varepsilon} \rho \frac{\varepsilon^2}{k} - R_\varepsilon + S_\varepsilon \quad (5)$$

$$G_k = -\rho \overline{u_i' u_j'} \frac{\partial u_j}{\partial x_i} = \mu_t S^2 \quad (6)$$

$$G_b = \beta g \frac{\mu_t}{Pr_t} \frac{\partial T}{\partial x_i} \quad (7)$$

where  $S_k$  and  $S_\varepsilon$  are user defined source terms, which are neglected.  $C_{1\varepsilon}$  and  $C_{2\varepsilon}$  are constants and they are equal to 1.42 and 1.68, respectively.  $G_k$  and  $G_b$  is [40] generation of

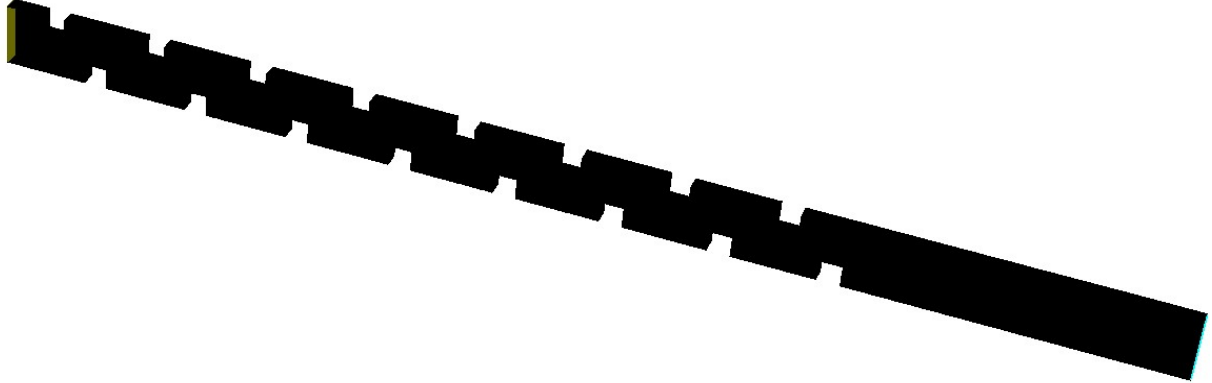


Figure 3 Numerical model of channel

$S$  in Eq. 6 is the modulus of the mean rate of strain tensor with respect to Boussinesq hypothesis for calculation of  $G_k$ , which is given in Eq. 8.

$$S = \sqrt{2S_{ij}S_{ij}} \quad (8)$$

$Pr_t$  in Eq. 7 is turbulent Prandtl number and it is given in Eq. 9.

$$Pr_t = \frac{1}{\alpha} \quad (9)$$

where  $\alpha$  in Eq. 9 is calculated from the below equation, which includes a constant number of  $\alpha_0$ , is equal to 1.

$$\left| \frac{\alpha - 1.3929}{\alpha_0 - 1.3929} \right|^{0.6321} \left| \frac{\alpha + 2.3929}{\alpha_0 + 2.3929} \right|^{0.3679} = \frac{\mu_{mol}}{\mu_{eff}} \quad (10)$$

$\beta$  in Eq. 7 is coefficient of thermal expansion and it is given in Eq.10.

$$\beta = -\frac{1}{\rho} \left( \frac{\partial \rho}{\partial T} \right)_p \quad (11)$$

$C_{3\varepsilon}$  in Eq. 5 is a constant and affects  $\varepsilon$  with respect to buoyancy effects. It is given in Eq. 12.

$$C_{3\varepsilon} = \tanh \left| \frac{v}{u} \right| \quad (12)$$

$v$  and  $u$  represents velocity of parallel and perpendicular vectors to gravitational vectors. However gravity effects are neglected in this analyses, hence effects of buoyancy is neglected.  $Y_M$  in Eq. 4 represents the contribution of fluctuating dilatation in compressible turbulence to overall dissipation rate and it is given in Eq. 13.

$$Y_M = 2\rho \varepsilon M_t^2 \quad (13)$$

where  $M_t$  represents turbulent Mach number and it given in Eq. 14.

$$M_t = \sqrt{\frac{k}{a^2}} \quad (14)$$

$a$  is used as speed of sound and it is approximately equal to  $\sqrt{\rho RT}$ , meanwhile the usage of  $Y_M$  is neglected in this analysis. Because of compressible turbulent effects are neglected. Effective viscosity ( $\mu_{eff}$ ) in Eq. 4 and 5 is calculated for low Reynolds number and near wall flows are given in Eq. 15,

$$d \left( \frac{\rho^2 k}{\sqrt{\varepsilon \mu}} \right) = 1.72 \frac{\hat{v}}{\sqrt{\hat{v}^3 - 1 + C_v}} d\hat{v} \quad (15)$$

$\tilde{\nu}$  in Eq. 15 is equal to  $\mu_{eff}/\mu$  and  $C_v$  nearly equals to 100. If high Re limits are used,  $\mu_t$ , which is same condition as effective viscosity, is given in Eq. 16.

$$\mu_t = \rho C_\mu \frac{k^2}{\varepsilon} \quad (16)$$

$C_\mu$  is equal to 0.0845.  $R_\varepsilon$  in Eq. 4, which mainly differs RNG from standard k-epsilon, is given in Eq. 17.

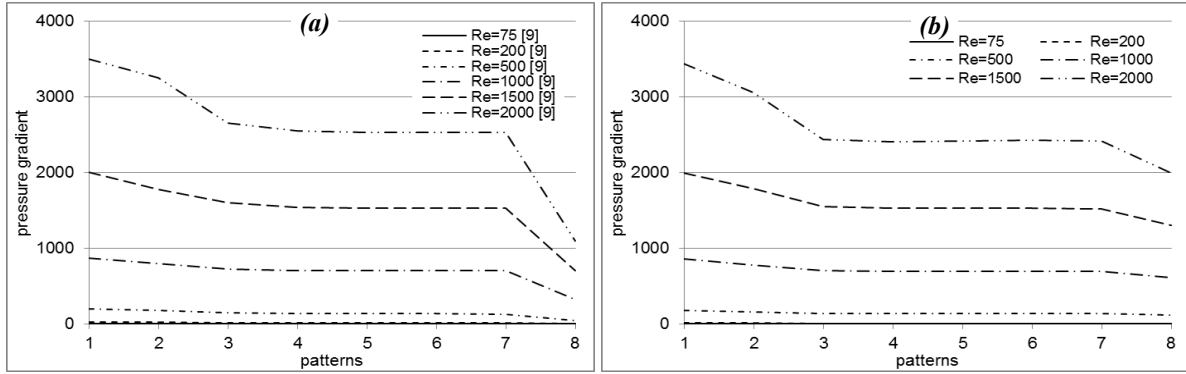


**Figure 4** Effect of Re on pressure changes of argon with respect to patterns for, (a) the compared study results [9], (b) this study results

$$R_\varepsilon = \frac{C_\mu \rho \eta^3 \left(1 - \frac{\eta}{\eta_0}\right) \varepsilon^2}{1 + \beta \eta^3} \quad (17)$$

In Eq. 17,  $\eta = Sk / \varepsilon$ ,  $\eta_0 = 4.38$  and  $\beta = 0.012$ . More detailed information can be achieved in theory guide [38] and literature.

Pressure or forces, which act on wall surfaces, are directly imported to ANSYS mechanical for strength analysis. Surfaces can be modelled with shell or solid elements. Shell181 element [41] is used in ANSYS with respect to thickness. Finite element model of wall surfaces have same geometrical sizes as the used grid elements in FLUENT. Shell181 element consists of 4 node structure shells and is used in 3D shell analyses.

Aluminium can be classified ductile materials. Hence the stress results are considered with Tresca (maximum shear stress) theory. The yield of material [42] begins with achieving of maximum shear stress of material and it is given in Eq. 18.

$$\tau_{tresca} = \frac{\sigma_1 - \sigma_3}{2} \quad (18)$$

where  $\sigma_1$  and  $\sigma_3$  are maximum and minimum principal stresses. Strength of materials is investigated with Tresca yield stress theory in this analysis.

## RESULTS AND DISCUSSIONS

Solution results includes pressure distribution, streamlines of velocity profile, vortex and stress formation locations and

distribution of stresses on inner surfaces of upper and lower ribs. All these impressions show general characteristics of flow characteristics and vortex formations of fluid and stress formations inside and on the channel.

In Fig. 4, comparison of pressure drop results between gained results and compared study [9]. The results yield with the compared study [9] without the last pattern, which is under the effect of outlet pressure. Velocity patterns comparison this study results and the compared [9] study are also available in another study [43], which have perfect agreement between each other. The first four patterns have more importance and the results can be acceptable for this study. It is observed that a rapid pressure gradient decrease occurs on first and second patterns. Other patterns have nearly constant results. Increasing the Re causes to increase pressure gradient. Other fluids' pressure drop characteristics are given with considering Nusselt number results in another study of this study. In general, Nusselt number and pressure drop results both given in literature studies.

Pressure contours of argon, water and nanofluid are given from centre plane of channel for investigation the effect of different Re in Fig. 5, 6 and 7, respectively. Same pressure distributions are observed in all solution of different fluids when Re is equal to 75. Each pattern includes a pressure region ( $P_{region}$ ), which follow the other pressure region ( $P_{region}$ ) with decreasing values in sequence. Only first pattern has differences from other patterns, which is under the dominant effect of inlet velocity. The upper surfaces of below ribs have lower pressure region ( $P^-$ ) in related patterns in argon solutions. Higher pressure

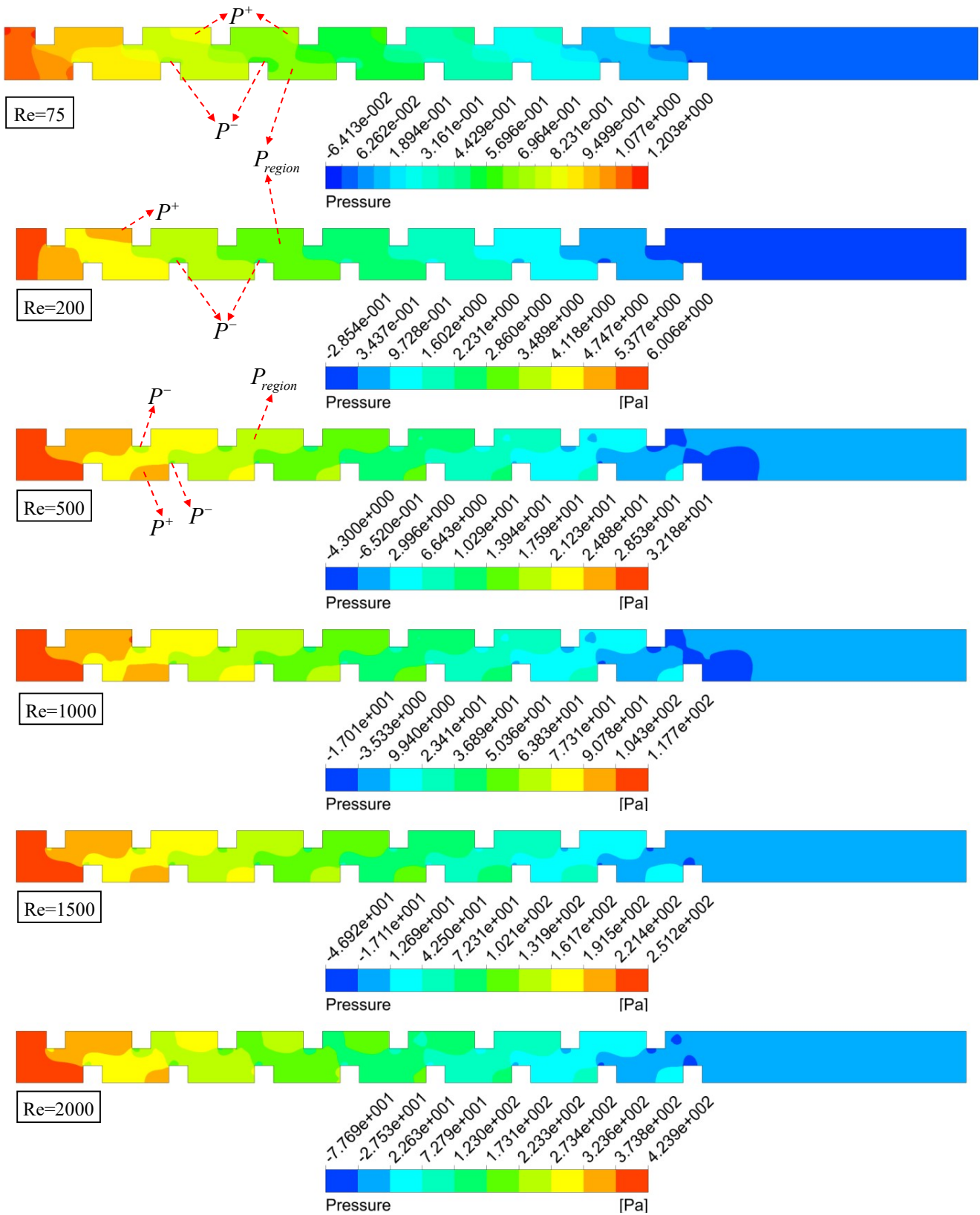
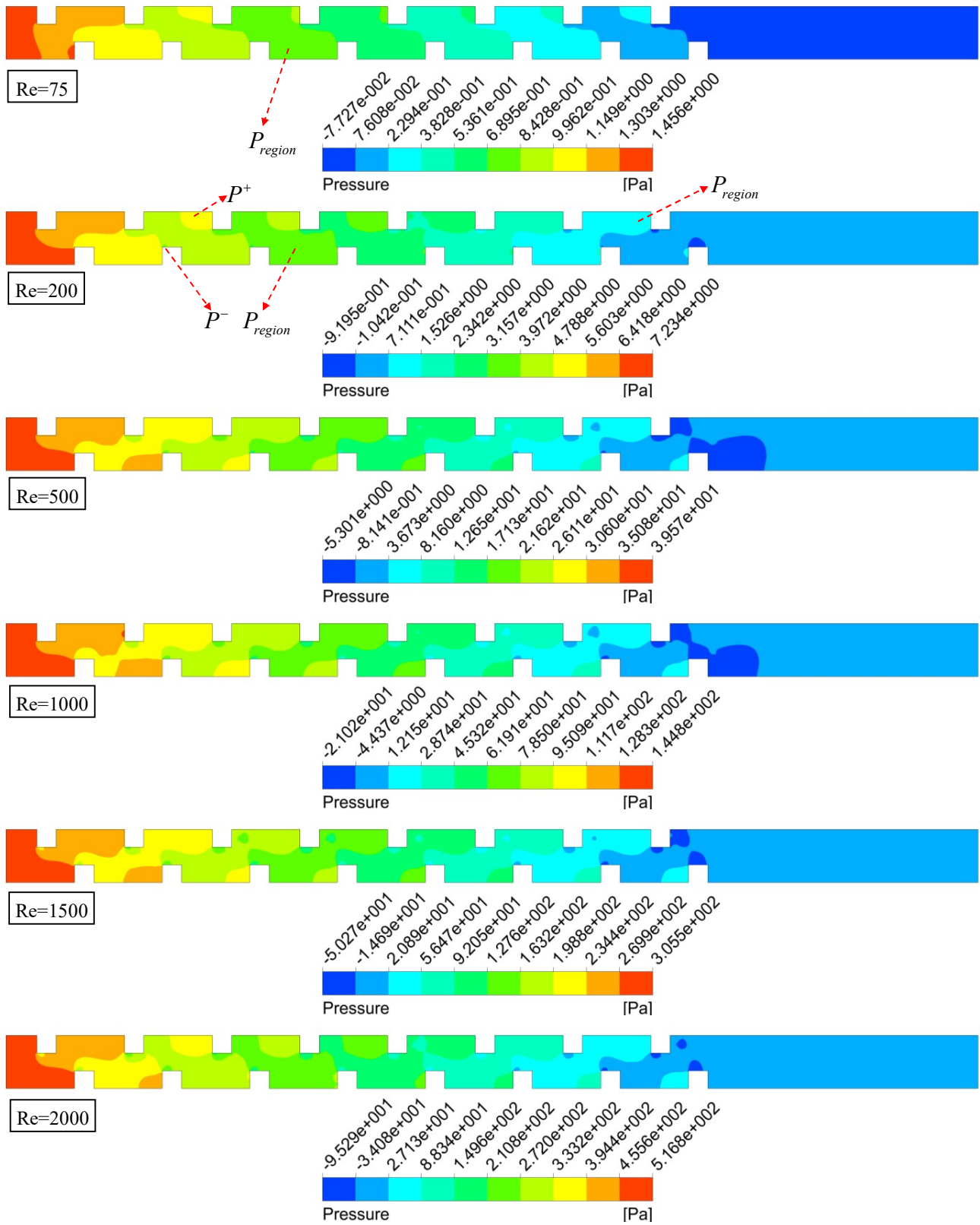
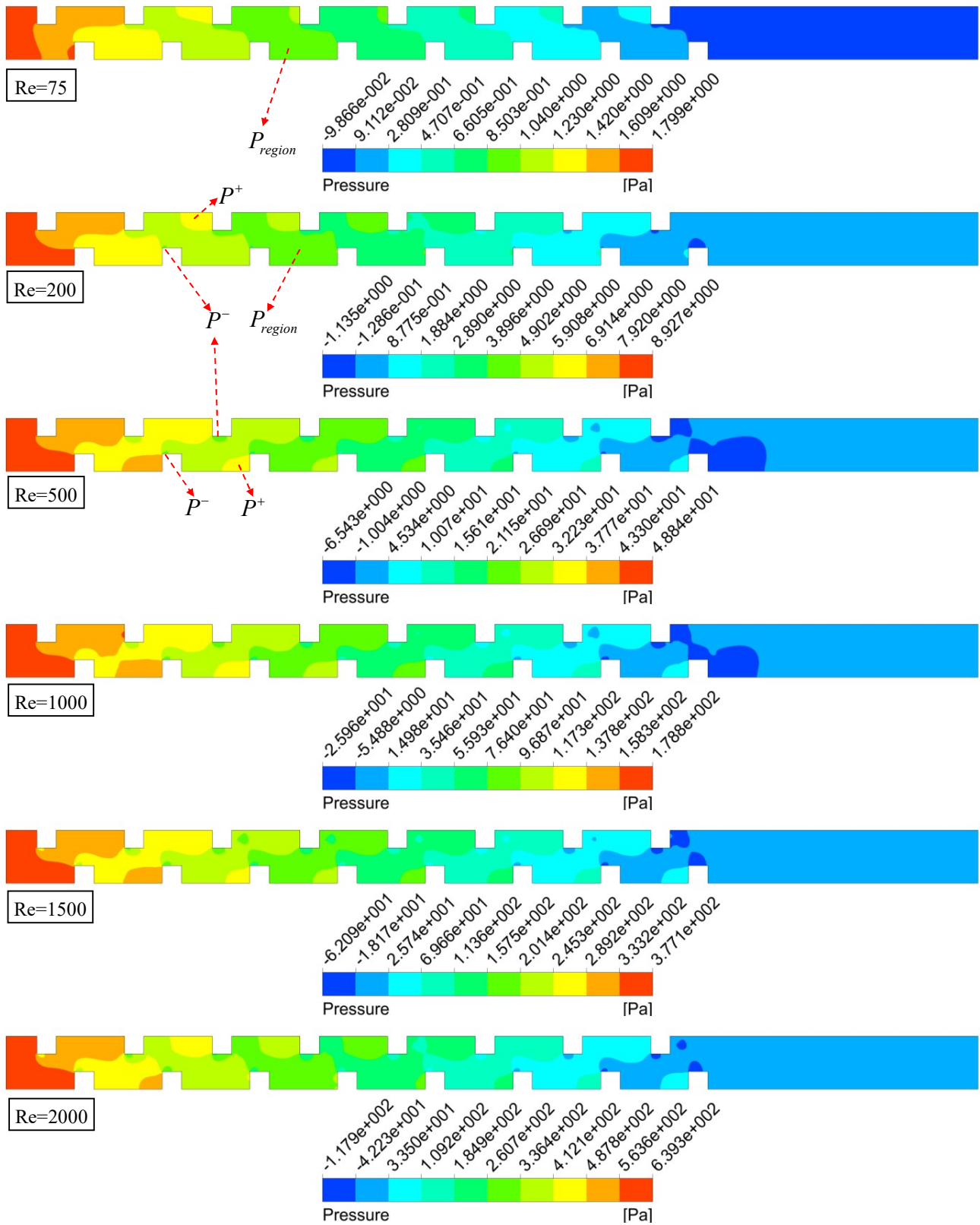


Figure 5 Pressure contours of argon at the centre plane of channel for different Reynolds numbers



**Figure 6** Pressure contours of water at the centre plane of channel for different Reynolds numbers



**Figure 7** Pressure contours of nanofluid at the centre plane of channel for different Reynolds numbers

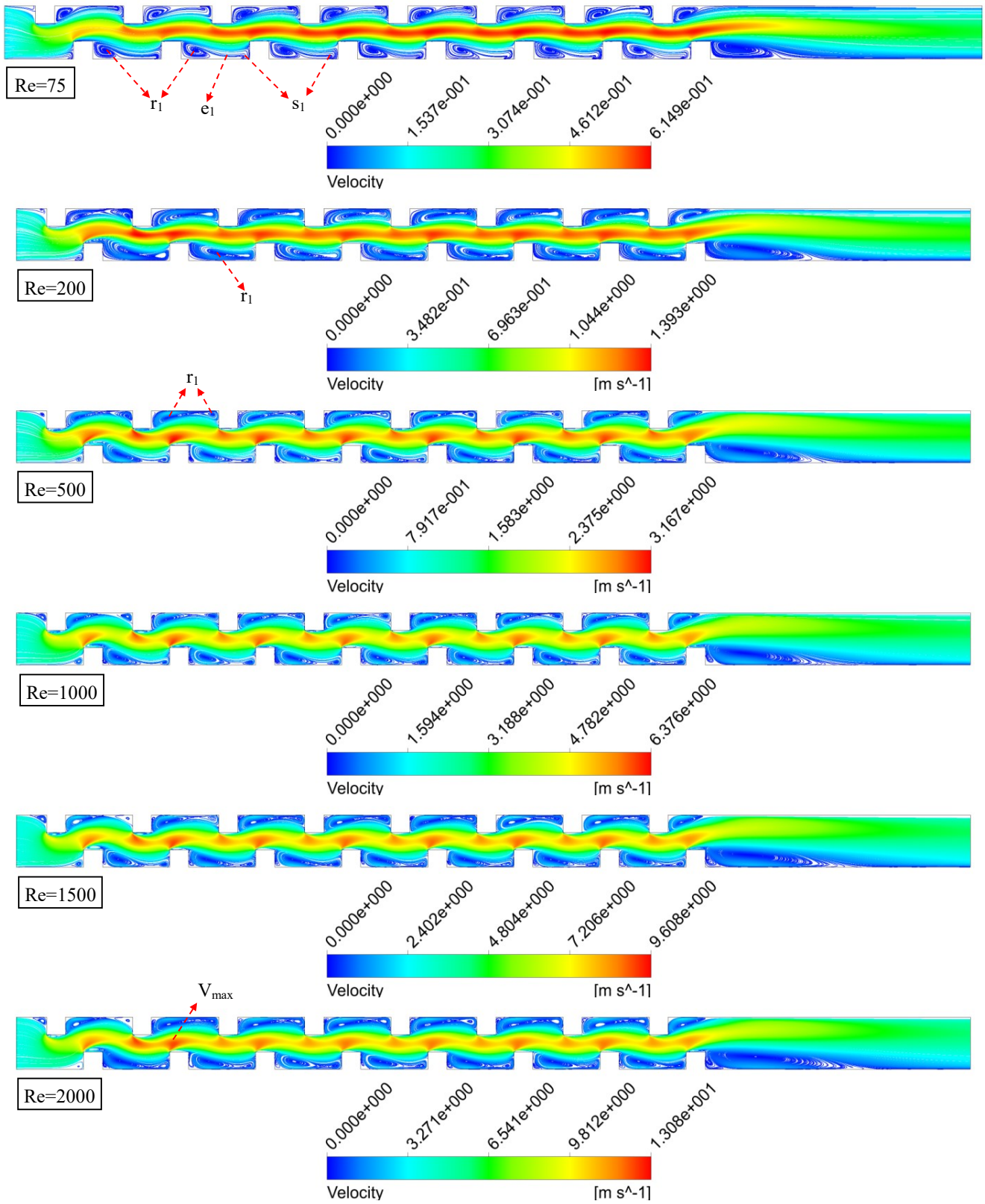


**Figure 8** Streamlines of argon at the centre plane of channel for different Reynolds numbers

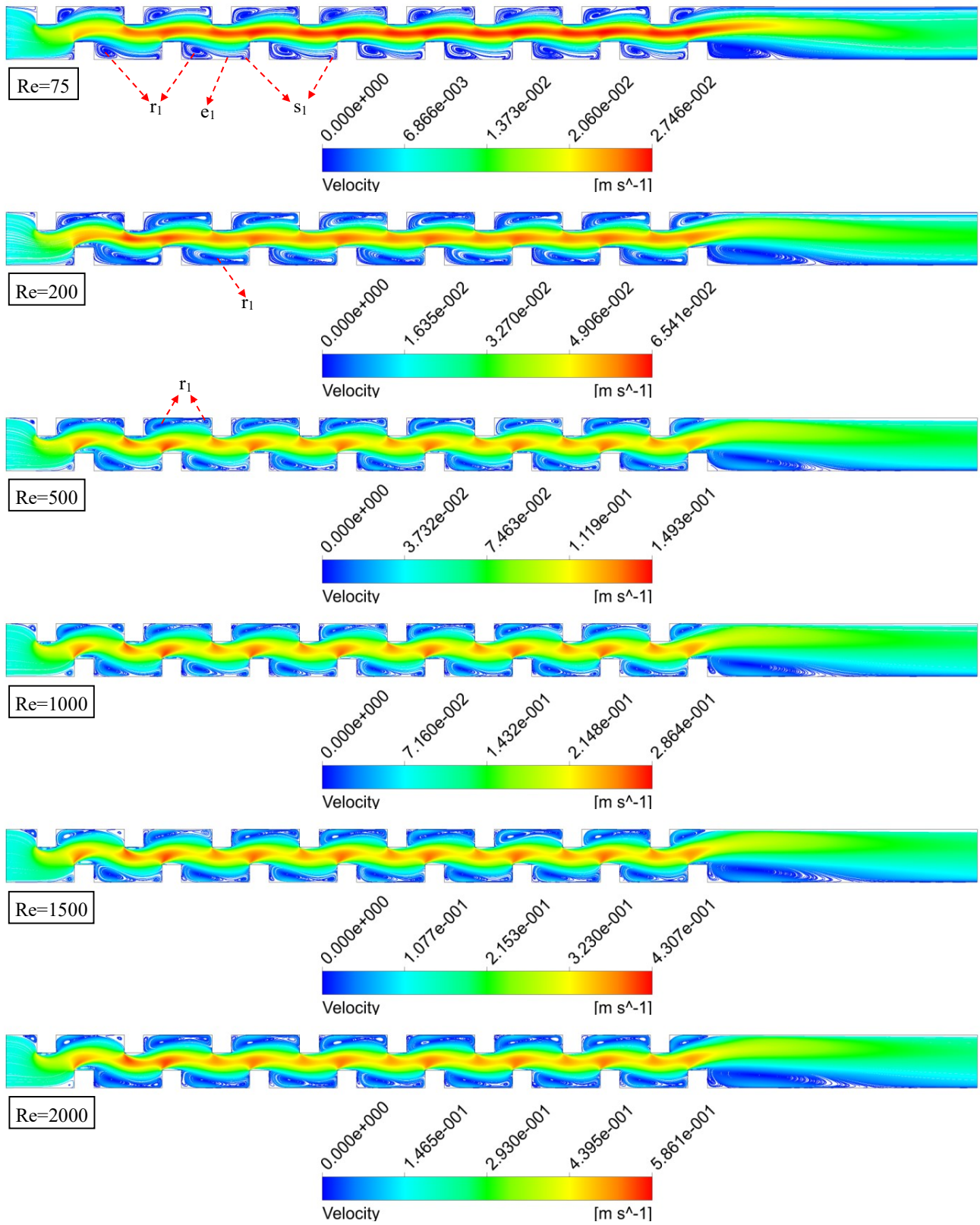


**Figure 9** Streamlines of water at the centre plane of channel for different Reynolds numbers

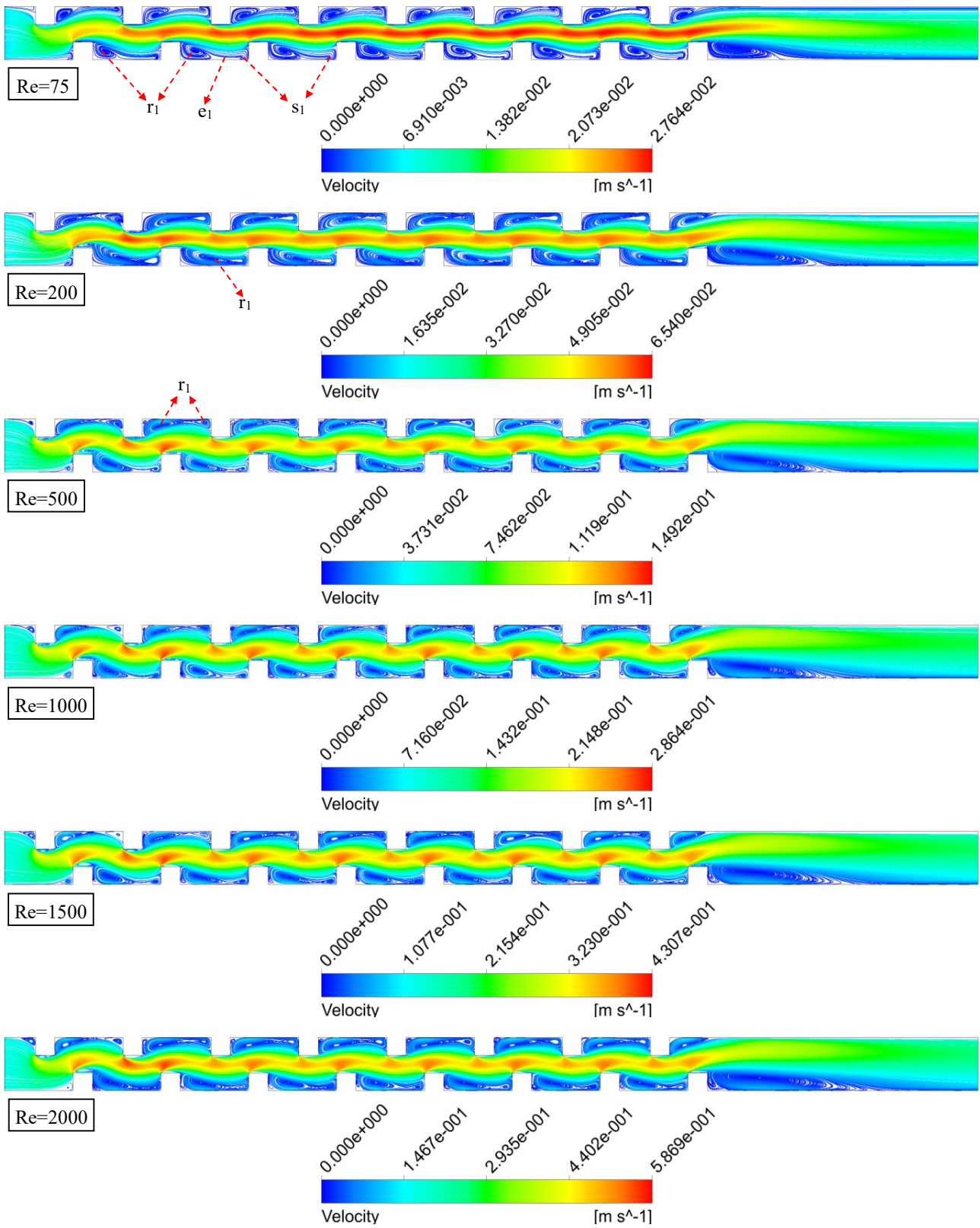


**Figure 10** Streamlines of nanofluid at the centre plane of channel for different Reynolds numbers

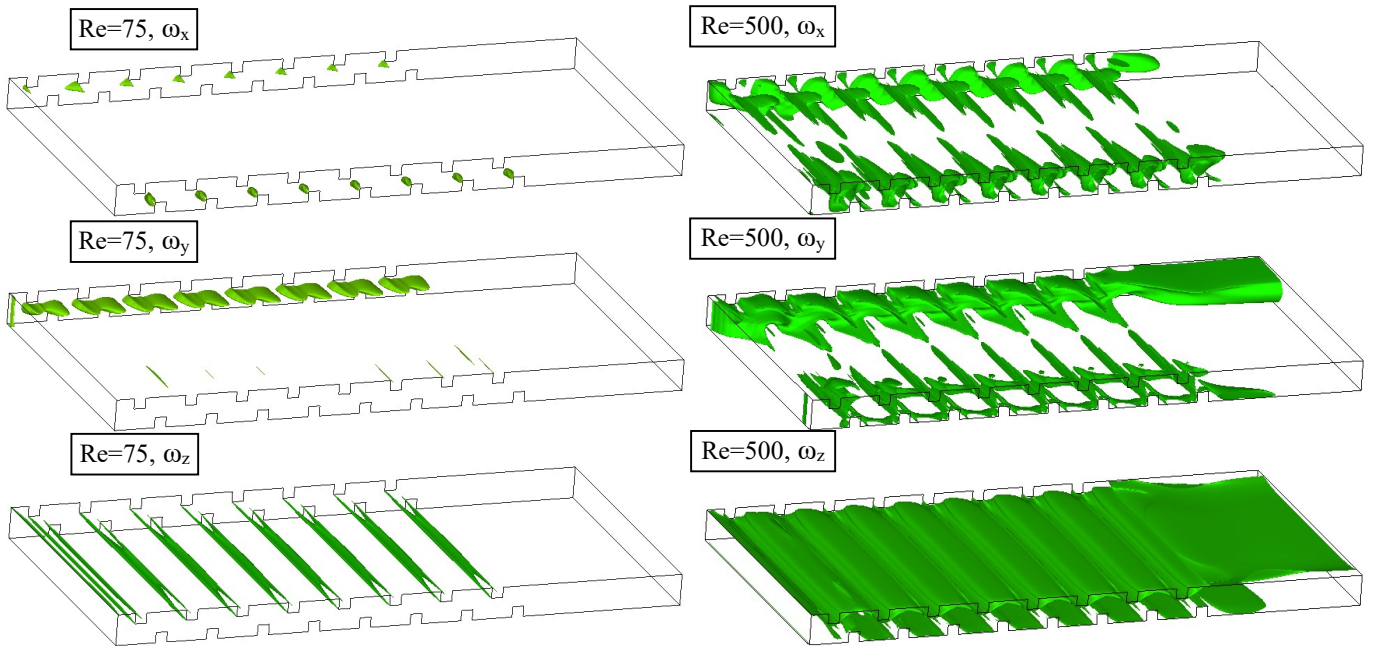


**Figure 11** Comparison of 400 value of  $\omega_x$ ,  $\omega_y$  and  $\omega_z$  vorticity locations for argon flow at Reynolds numbers of 75 and 500

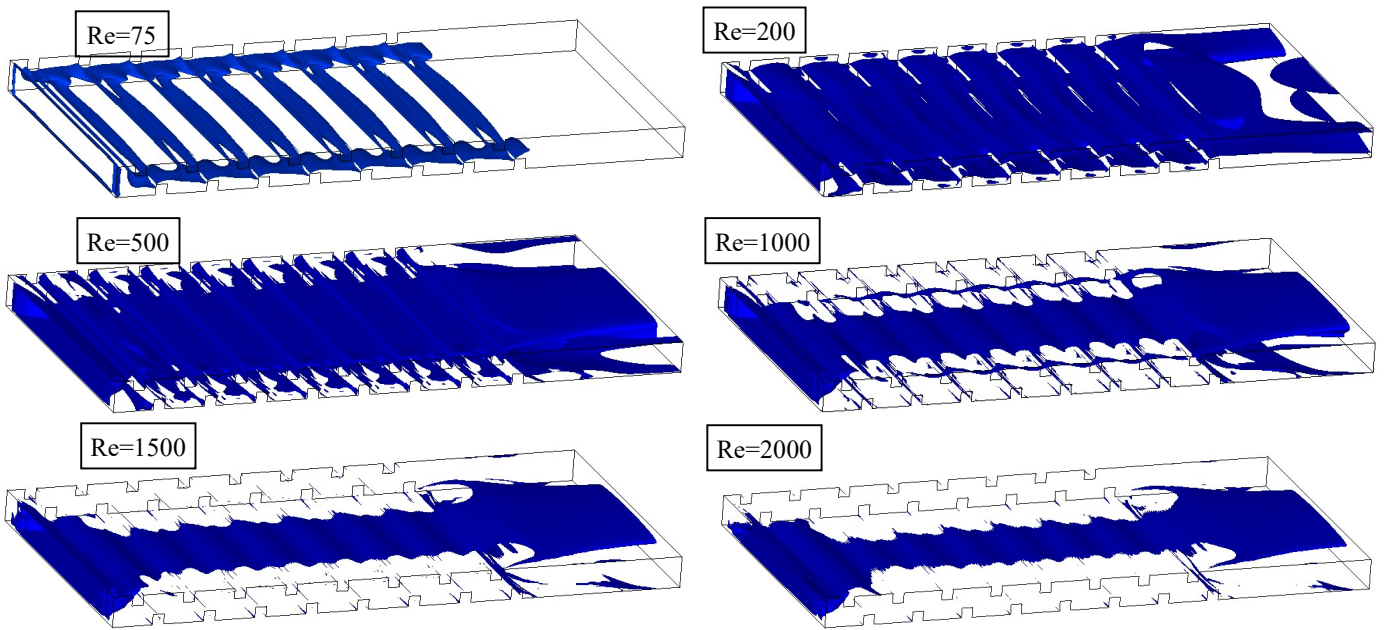


**Figure 12** 400 value of vorticity magnitude for argon flow at different Reynolds numbers

region ( $P^+$ ) is observed at the opposite of below ribs in all fluid flow solutions. These regions cover more places at the front side surface of upper ribs. The highest pressure occurs at the front side surface of first below rib.

Inlet velocity has dominant effect on first pattern, especially on below surfaces in all Re and different fluid flow solutions. When Re is equal to 200, pressure distribution changes between

argon and other fluids. Higher pressure region ( $P^+$ ) vanishes in argon solution at the upper surfaces. The profile appears similar as Re solution of 75 without high pressure regions ( $P^+$ ). However, pressure distribution of patterns does not follow in sequence, which begins difference at 6<sup>th</sup> pattern in water and nanofluid solutions. Their lower pressure region ( $P^-$ ) covered area is less than argon.

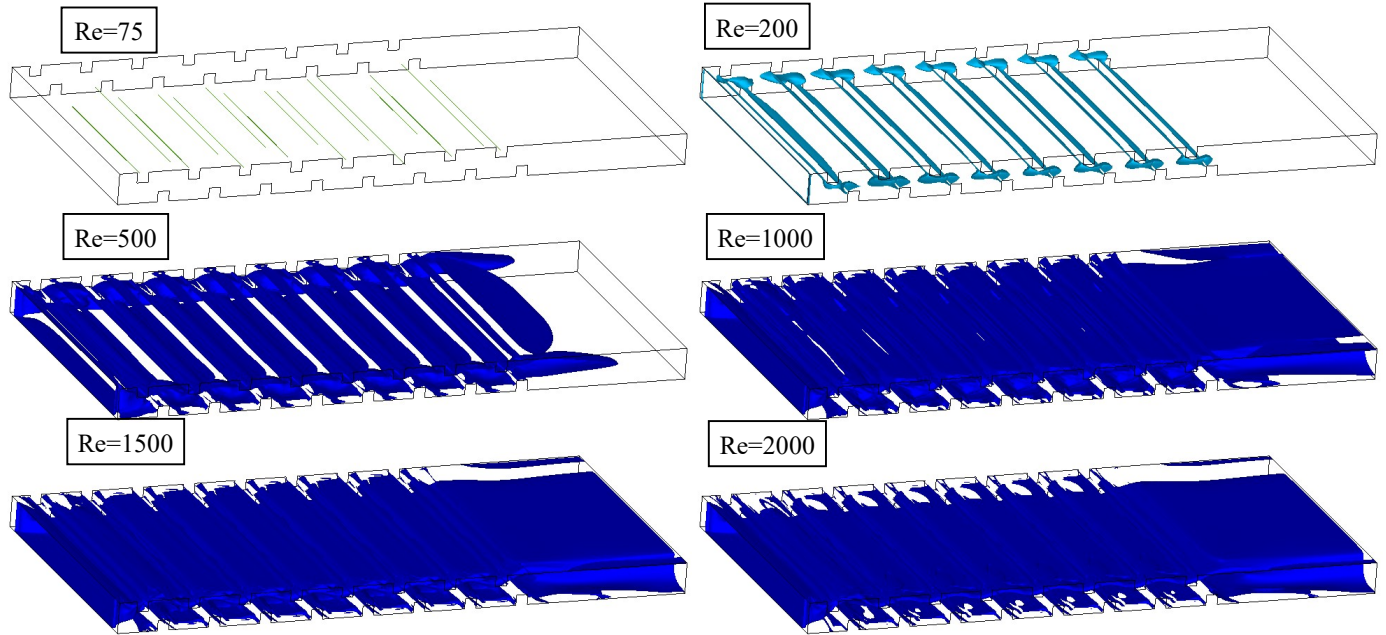


**Figure 13** 100 value of vorticity magnitude for water flow at different Reynolds numbers

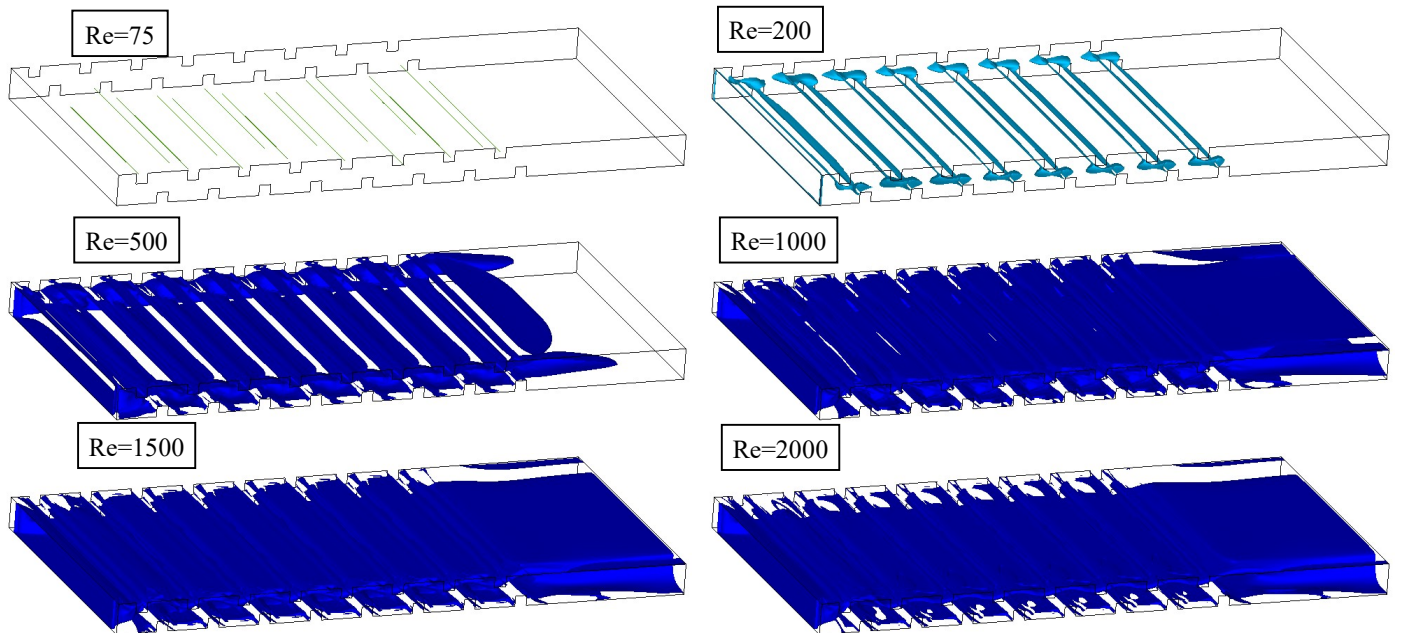


**Figure 14** 100 value of vorticity magnitude for nanofluid flow at different Reynolds numbers

Propagation of pressure region ( $P_{region}$ ) on argon changes when Re is increased to 500. A low pressure region ( $P^-$ ) occurs on upper surface of upper ribs and front edge of below ribs. Higher pressure region ( $P^+$ ) occurs at the front side of below ribs. This pressure profile nearly becomes constant, even if Re is increased from 500 to 2000 in argon solutions.

However, pressure region ( $P_{region}$ ) propagation changes in water and nanofluid solutions when Re is increased to 500. Higher pressure region ( $P^+$ ) vanishes at the front side of upper ribs and occurs at front side of below ribs. This profile behaviour is constant up to Re of 2000. When the used Re is equal to 2000, pressure region ( $P_{region}$ ) begins to change, especially at the 6<sup>th</sup> pattern. Pressure values increase with increasing Re in all fluid

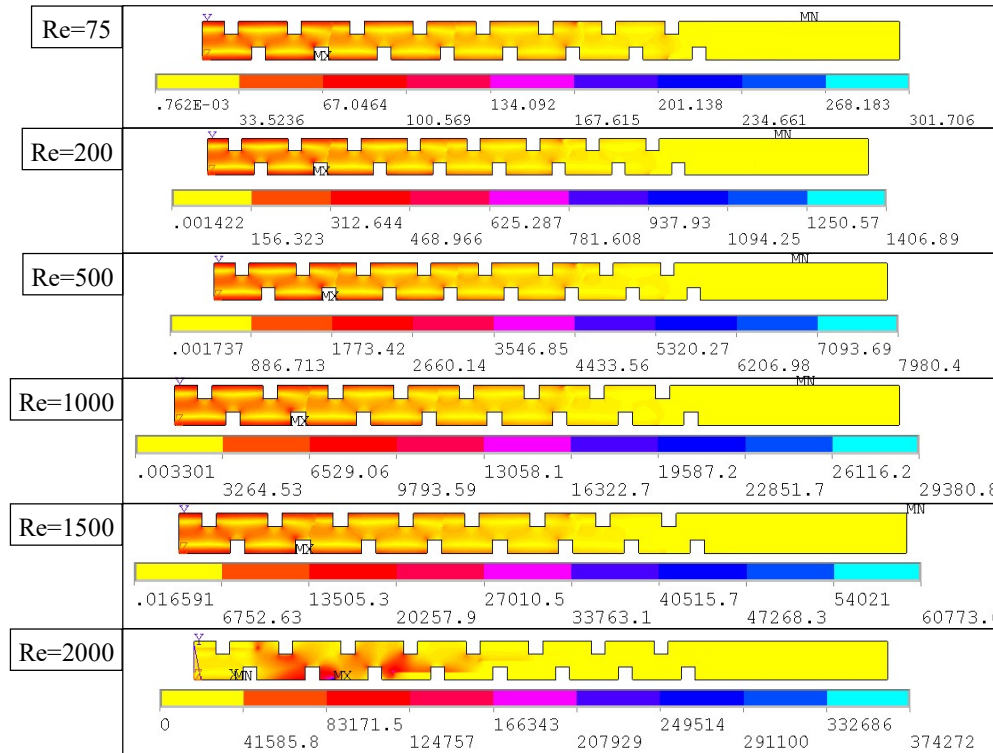


Figure 15 Tresca stress contours of channel surface for argon at different Reynolds numbers

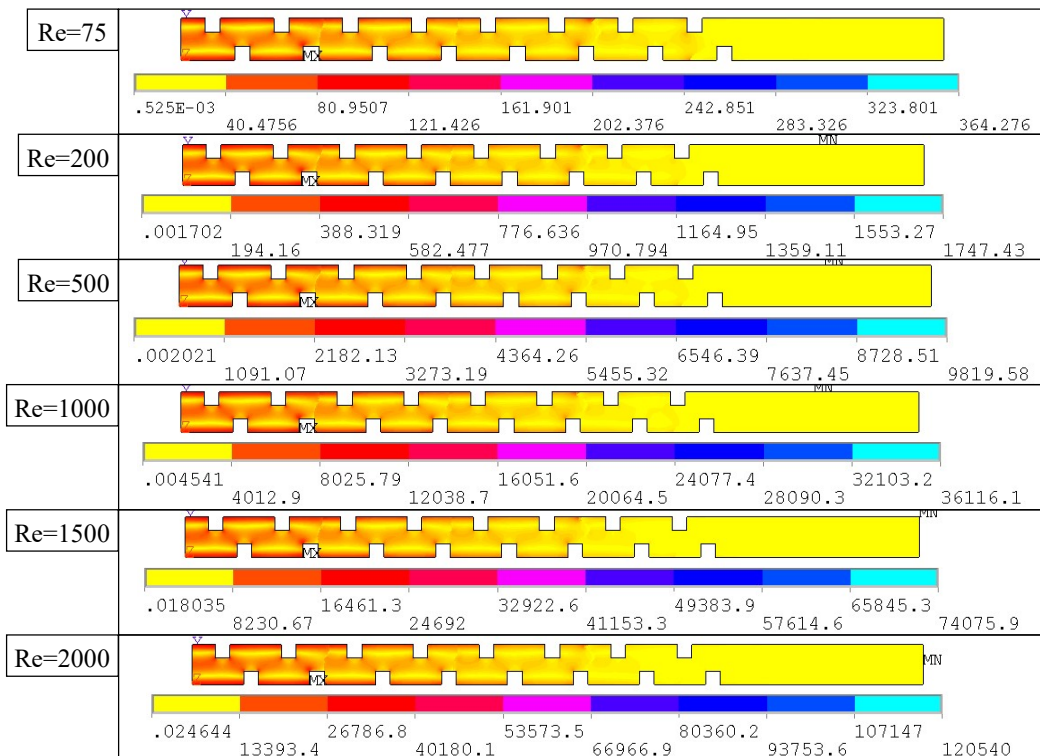


Figure 16 Tresca stress contours of channel surface for water at different Reynolds numbers

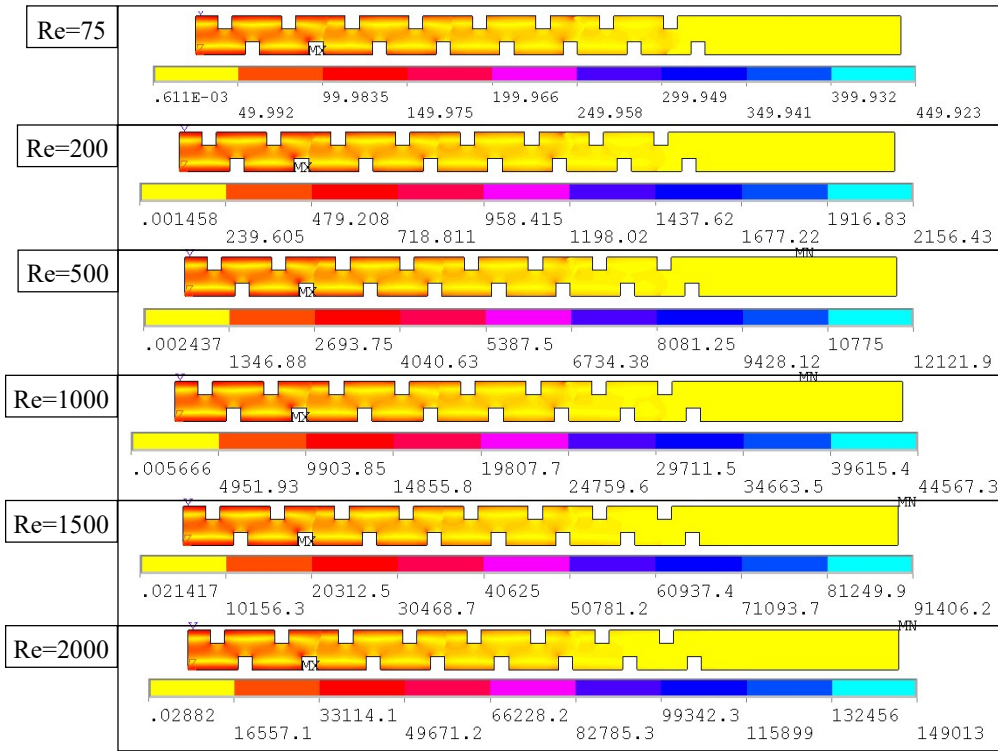


Figure 17 Tresca stress contours of channel surface for nanofluid at different Reynolds numbers

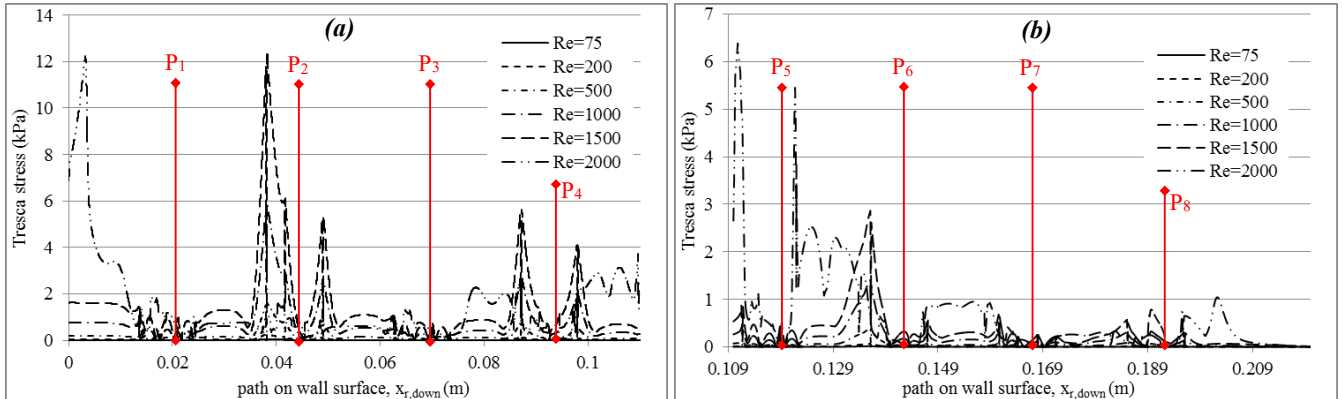


Figure 18 Tresca stress results of channel for argon at different Reynolds numbers along path of  $x_{r,down}$ ; (a) left side, (b) right side

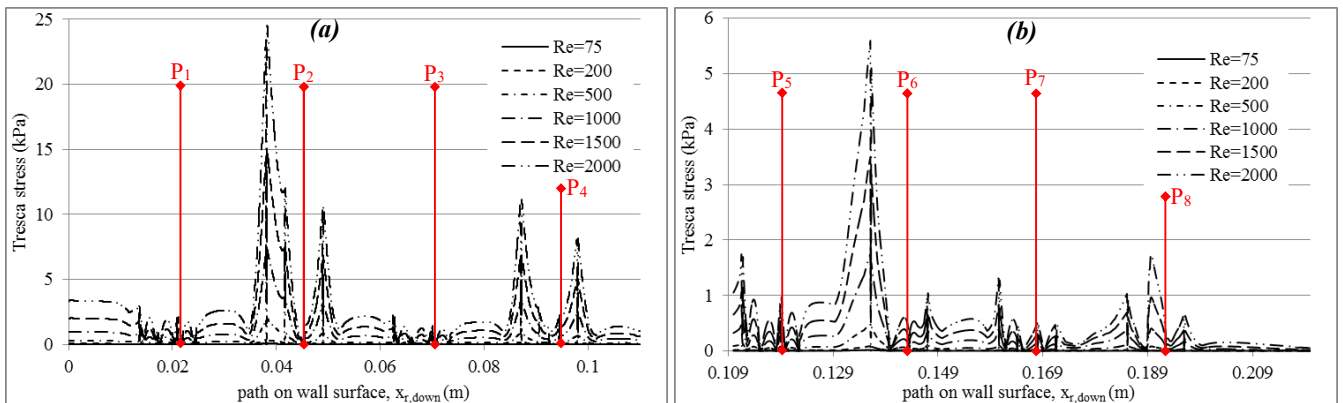
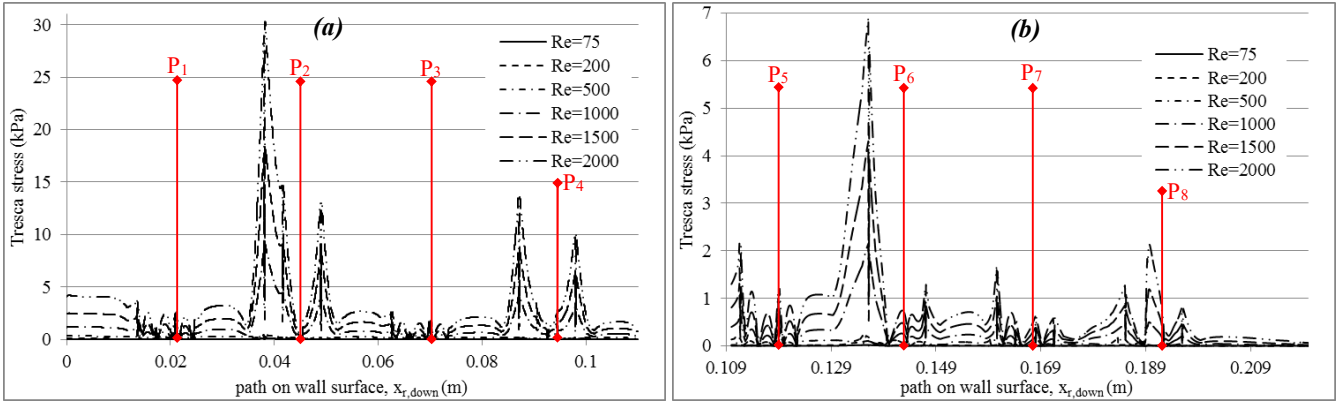
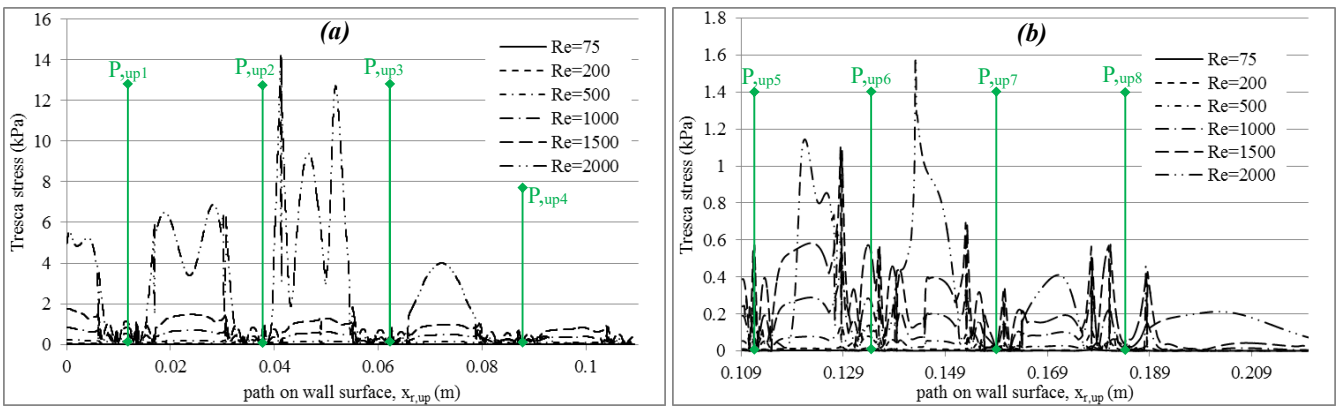


Figure 19 Tresca stress results of channel for water at different Reynolds numbers along path of  $x_{r,down}$ ; (a) left side, (b) right side



**Figure 20** Tresca stress results of channel for nanofluid at different Reynolds numbers along path of  $x_{r,down}$ ; (a) left side, (b) right side



**Figure 21** Tresca stress results of channel for argon at different Reynolds numbers along path of  $x_{r,up}$ ; (a) left side, (b) right side

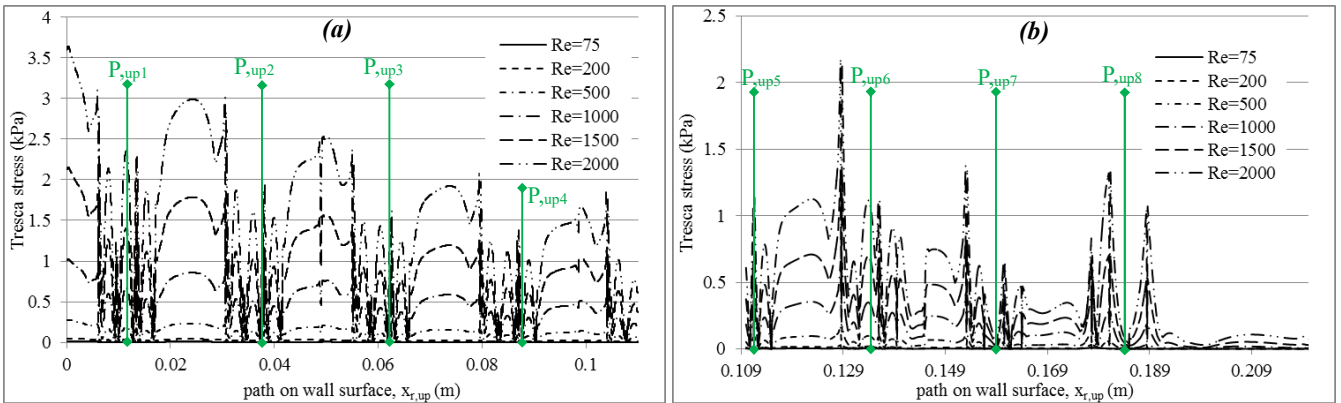


**Figure 22** Tresca stress results of channel for water at different Reynolds numbers along path of  $x_{r,up}$ ; (a) left side, (b) right side

flow solutions. Nanofluid solutions have the highest pressure values, which may occur from its highest density in the analysed fluids.

Velocity profiles of solutions are illustrated in Fig. 8, 9 and 10. Even if different fluids and velocities are used in solutions, their used Re are same, which supports to behave similar flow and vortex formation characteristics. Hence only difference occurs with respect to Re. When the used Re is equal to 75, laminar

flow solutions are used, which affects flow separation behaviour and vortex formations.

A vortex core ( $r_i$ ) is observed behind the each rib. The core ( $r_i$ ) have been fed along the groove flow and has a path of recirculation ( $e_i$ ), which starts from a stagnation point ( $s_i$ ) in Re resolutions of 75. Flow separation locations are observed upper surfaces of ribs. When Re is used as 200, vortex core ( $r_i$ ) gets widespread. The path ( $e_i$ ) gets recirculation and stagnation

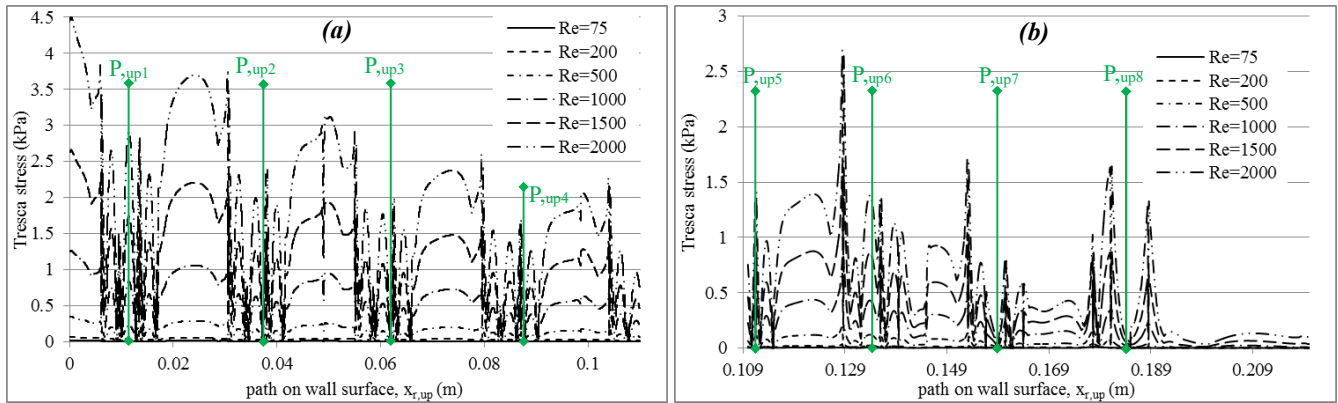


**Figure 23** Tresca stress results of channel for nanofluid at different Reynolds numbers along path of  $x_{r,up}$ ; (a) left side, (b) right side

point ( $s_1$ ) disappears from surface of channel. Flow which passes centre of the plane disturbs with increasing Re. Two vortex cores are observed in grooves, behind the ribs, when Re is increased to 500. A small vortex structure occurs behind side surface of ribs. The vortex, which occurs behind 8<sup>th</sup> rib, gets widespread with increasing Re. Maximum velocity locations are detected between 1<sup>st</sup> and 2<sup>nd</sup> ribs.

In Fig. 11, iso-surface of x, y and z direction of vortices are given for Re of 75 and 500. The effect of Re increment can be observed for locations of vortex formations. When Re number is equal to 75, x direction vortices occur at the front edge of ribs, near the side channel walls. y direction vortices occur as similar as x direction vortices. However, they gather at one of side surface of the each rib in the channel. z direction vortices occur at the front edges of ribs, along from one side to other side of channel. They occur more at the centre of ribs' front edge. When Reynolds number is increased to 500, their covered regions get larger. x direction vortices get enlarge symmetrically with other side surfaces, on the ribs. y direction vortices also occur other side surface of channel, but less than initial formation side surface. z direction vortices have the greatest region for iso-surface value of 400.

In Fig. 12, 13 and 14, vorticity magnitude values of 400, 100 and 100 are given for argon, water and nanofluid, respectively. Vortex values and their magnitudes get larger with

Increasing Reynolds number. The constant and only value of 400 of vorticity magnitude occur at different locations. At first, they occur only on ribs and their near locations between one sides to other side of the channel. However when Reynolds number increases, they cover beyond side of 8<sup>th</sup> ribs. Its density at the side surfaces of channel decreases and they only form at the centre location of channel. When iso-surface of 100 value of vorticity magnitude is considered in water and nanofluid solution, it is observed that they occur at front edge of ribs, along between side surfaces of channel. Their sizes get increasing with increasing Reynolds number. Water and

nanofluid flow results cover more region than argon. The density of vortices decreases at side surfaces of channel.

Tresca stress results are given in Fig. 15, 16 and 17 for argon, water and nanofluid solutions. High stress locations occur nearly at the 1<sup>st</sup>, 2<sup>nd</sup>, 3<sup>rd</sup> and 4<sup>th</sup> rib edges and groove surfaces. When Reynolds number increases, values of occurred stresses get increasing, especially at the first four ribs. The highest stress occurs at the near locations of 2<sup>nd</sup> below rib sides. Stresses are increasing nonlinearly. Low stress region occurs on smooth wall channels after the 8<sup>th</sup> rib. Non-uniform stress distribution can cause stress peak points and high stress locations, which should be eliminated with suitable design operations. The results of nanofluid have the highest values without the results of Re of 2000. When Re is equal to 2000, the highest stress results occur at argon solutions.

In Fig. 18, 19 and 20, Tresca stress results are given for along path of  $x_{r,down}$ . The path results are given into two parts; a and b, for providing the observation of stresses easily. Nearly the first half of the channel is represented with a and other half is represented as b.

Stress distributions of both analysed conditions (for argon, water and nanofluid) have similar characteristics. Nanofluid flow solutions have the highest stress results, which occur between 1<sup>st</sup> and 2<sup>nd</sup> patterns. They occur, when Re is used as 2000. First four patterns have greater stress results (in Fig. 18.a, 19.a, 20.a) than other patterns. Some high stress peak points occur, which may be caused from sharp corners of ribs and groove ends. The peak stress values of argon is nearly half of water and nanofluid on the path of  $x_{r,down}$ .

In Fig. 21, 22 and 23, Tresca stress results are given for along path of  $x_{r,up}$ . It is observed that stress values are less than along path of  $x_{r,down}$ . Argon solution of Re of 2000 has high stress distributions. Without these results, the highest stresses occur at nanofluid flow solutions. The results get decreases when fluid passes patterns to outlet location.

## CONCLUSION

In this study, effects of ribs in a rectangular channel are investigated on flow characteristics of a nanofluid. Stress formations are illustrated. Channel is formed with 8 repeated same patterns and each patterns effect on flow characteristics and stress formations are discussed. The gained knowledge in this study can be summarized as;

- The upper surfaces of below ribs have lower pressure region ( $P^-$ ) in related patterns
- Higher pressure region ( $P^+$ ) is observed at the opposite of below ribs
- The highest pressure occurs at the front side surface of first below rib
- Inlet velocity has dominant effect on first pattern, especially on below surfaces in all Reynolds number
- A vortex core ( $r_1$ ) is observed behind the each rib when Re is equal to 75
- Two vortex cores are observed in grooves, behind the ribs, when Re is increased to 500
- The vortices get widespread with increasing Reynolds number
- Maximum velocity locations are detected between 1<sup>st</sup> and 2<sup>nd</sup> ribs
- High stress locations occur nearly at the 1<sup>st</sup>, 2<sup>nd</sup>, 3<sup>rd</sup> and 4<sup>th</sup> rib edges and groove surfaces. When Reynolds number increases, values of occurred stresses get increasing. The highest stress occurs at the near locations of 2<sup>nd</sup> below rib sides
- Stress values of  $x_{r,up}$  are less than along path of  $x_{r,down}$
- The stresses on channel are less than yield stress of material, which provides safety
- Nanofluid has the highest pressure values and the highest stresses on the channel occur at nanofluid solutions. Meanwhile, the results of argon at Re of 2000 have greater stress values on the channel surface. However, in terms of general, it can be neglected.
- If safety of channel is considered, it is better to use argon rather than water and nanofluid.

Geometry of ribs will be investigated and optimized thickness of channel will be determined at the further stages of this study for achieving less stress concentration and flow separation locations. The determined stress peak points on the surfaces of channel will be decreased with suitable design operations.

## NOMENCLATURE

$\rho$	density of fluid [kg/m <sup>3</sup> ]
$c_p$	specific heat of fluid [J/kg.K]
$\lambda$	thermal conductivity of fluid [W/m.K]
$\mu$	dynamic viscosity of fluid [kg/m.s]
$T_{walls}$	temperatures of walls [K]
$T_{inlet}$	inlet fluid temperature [K]
Re	Reynolds number [.]

$Re_c$	critical Reynolds number [.]
$D_h$	hydraulic diameter [m]
$V$	velocity of fluid at inlet [m/s]
$l_{sm}$	length of each module [m]
$h$	height of each module [m]
$w$	width of each module [m]
$l_r$	length of each rib [m]
$h_r$	height of each rib [m]
$w_r$	width of each rib [m]
$x_{r,up}$	results taken path on upper wall surface [m]
$x_{r,down}$	results taken path on lower wall surface [m]
$\lambda_{alu}$	thermal conductivity of aluminium
$\rho_{alu}$	density of aluminium [kg/m <sup>3</sup> ]
$c_{p,alu}$	specific heat of aluminium [J/kg.K]
$\tau_{y,tension}$	yield stress of aluminium in tension [MPa]
$\tau_{y, shear}$	yield stress of aluminium in shear [MPa]
$\tau_{ult,tension}$	ultimate stress of aluminium in tension [MPa]
$\tau_{ult, shear}$	ultimate stress of aluminium in shear [MPa]
$E$	Young's Modulus [GPa]
$\nu$	Poisson's ratio [.]
$\rho_{nano}$	density of nanofluid [kg/m <sup>3</sup> ]
$c_{p,nano}$	specific heat of nanofluid [J/kg.K]
$\lambda_{nano}$	thermal conductivity of nanofluid [W/m.K]
$\mu_{nano}$	dynamic viscosity of nanofluid [kg/m.s]
$k$	turbulent kinetic energy [m <sup>2</sup> /s <sup>2</sup> ]
$\epsilon$	turbulent dissipation rate [m <sup>2</sup> /s <sup>3</sup> ]
$S_k, S_\epsilon$	user defined source terms [.]
$C_{1\epsilon}, C_{2\epsilon}, C_{3\epsilon}$	turbulence model constants [.]
$G_k$	generation of turbulence kinetic energy for mean velocity gradient
$G_b$	generation of turbulence kinetic energy for buoyancy
$S$	modulus of the mean rate of strain tensor
$Pr_t$	turbulent Prandtl number [.]
$\alpha, \alpha_0$	a constant parameter [.]
$\beta$	coefficient of thermal expansion
$Y_M$	contribution of fluctuating dilatation in compressible turbulence
$M_t$	turbulent Mach number [Ma]
$a$	speed of sound [m/s]
$\mu_{eff}$	effective viscosity [Pa.s]
$C_{\mu, \eta, \eta_0}$	constants [.]
$r_1$	location of vortex core [.]
$e_1$	path of recirculation [.]
$s_1$	location of stagnation point [.]

## REFERENCES

- [1] X. Tang and D. Zhu, Experimental and numerical Study on heat transfer enhancement of a rectangular channel with discontinuous crossed ribs and grooves, *Chinese Journal of Chemical Engineering* **20(2)** (2012), 220-230.
- [2] S. Singh, S. Chander and J.S. Saini, Investigations on thermo-hydraulic performance due to flow-attack-angle in V-down rib with gap in a rectangular duct of solar air heater, *Applied Energy* **97** (2012), 907-912.

- [3] S. Skullong, S. Kwankaomeng, C. Thianpong and P. Promvonge, Thermal performance of turbulent flow in a solar air heater channel with rib-groove turbulators, *International Communications in Heat and Mass Transfer* **50** (2014), 34-43.
- [4] A.N. Al-Shamani, K. Sopian, H.A. Mohammed, S. Mat, M.H. Ruslan and A.M. Abed, Enhancement heat transfer characteristics in the channel with trapezoidal rib-groove using nanofluids, *Case Studies in Thermal Engineering* **5** (2015), 48-58.
- [5] H.T. Wang, W.B. Lee, J. Chan and S. To, Numerical and experimental analysis of heat transfer in turbulent flow channels with two-dimensional ribs, *Applied Thermal Engineering* **75** (2015), 623-634.
- [6] S. Pal and S.K. Saha, Laminar fluid flow and heat transfer through a circular tube having spiral ribs and twisted tapes, *Experimental Thermal and Fluid Science* **60** (2015), 173-181.
- [7] J. Liu, G. Xie and T.W. Simon, Turbulent flow and heat transfer enhancement in rectangular channels with novel cylindrical grooves, *International Journal of Heat and Mass Transfer* **81** (2015), 563-577.
- [8] H.A. Mohammed, A.N. Al-Shamani and J.M. Sheriff, Thermal and hydraulic characteristics of turbulent nanofluids flow in a rib-groove channel, *International Communications in Heat and Mass Transfer* **39** (2012), 1584-1594.
- [9] T. Desrues, P. Marty and J.F. Fourmigue, Numerical prediction of heat transfer and pressure drop in three-dimensional channels with alternated opposed ribs, *Applied Thermal Engineering* **45-46** (2012), 52-63.
- [10] P. Promvonge and C. Thianpong, Thermal performance assessment of turbulent channel flows over different shaped ribs, *International Communications in Heat and Mass Transfer* **35** (2008), 1327-1334.
- [11] Sunil Chamoli, N.S. Thakur and J.S. Saini, A review of turbulence promoters used in solar thermal systems, *Renewable and Sustainable Energy Reviews* **16** (2012), 3154-3175.
- [12] T. Alam, R.P. Saini and J.S. Saini, Use of turbulators for heat transfer augmentation in an air duct - A review, *Renewable Energy* **62** (2014), 689-715.
- [13] S. Tamna, S. Skullong, C. Thianpong and P. Promvonge, Heat transfer behaviors in a solar air heater channel with multiple V-baffle vortex generators, *Solar Energy* **110** (2014), 720-735.
- [14] K. Kulkarni, A. Afzal and K. Kim, Multi-objective optimization of solar air heater with obstacles on absorber plate, *Solar Energy* **114** (2015), 364-377.
- [15] P. Sriromreun, C. Thianpong and P. Promvonge, Experimental and numerical study on heat transfer enhancement in a channel with Z-shaped baffles, *International Communications in Heat and Mass Transfer* **39** (2012), 945-952.
- [16] P. Promvonge, C. Khanoknaiyakarn, S. Kwankaomeng and C. Thianpong, Thermal behavior in solar air heater channel fitted with combined rib and delta-winglet, *International Communications in Heat and Mass Transfer* **38** (2011), 749-756.
- [17] L. Al-Hadhrami and J. Han, Effect of rotation on heat transfer in two-pass square channels with five different orientations of 45 angled rib turbulators, *International Journal of Heat and Mass Transfer* **46** (2003), 653-669.
- [18] V. Kongkaiptaiboon, K. Nanan and S. Eiamsa-ard, Experimental investigation of heat transfer and turbulent flow friction in a tube fitted with perforated conical-rings, *International Communications in Heat and Mass Transfer* **37** (2010), 560-567.
- [19] A. Durmus, Heat transfer and exergy loss in cut out conical turbulators, *Energy Conversion and Management* **45** (2004), 785-796.
- [20] S.A. Isaev, N.V. Kornev, A.I. Leontiev and E. Hassel, Influence of the Reynolds number and the spherical dimple depth on turbulent heat transfer and hydraulic loss in a narrow channel, *International Journal of Heat and Mass Transfer* **53** (2010), 178-197.
- [21] W. Ji, A.M. Jacobi, Y. He and W. Tao, Summary and evaluation on single-phase heat transfer enhancement techniques of liquid laminar and turbulent pipe flow, *International Journal of Heat and Mass Transfer* **88** (2015), 735-754.
- [22] Z. Li, Y. Wu, G. Tang, D. Zhang and J. Lu, Comparison between heat transfer to supercritical water in a smooth tube and in an internally ribbed tube, *International Journal of Heat and Mass Transfer* **84** (2015), 529-541.
- [23] X. Tang and D. Zhu, Flow structure and heat transfer in a narrow rectangular channel with different discrete rib arrays, *Chemical Engineering and Processing: Process Intensification* **69** (2013), 1-14.
- [24] J.M. Calm, The next generation of refrigerants-historical view, considerations, and outlook, *International Journal of Refrigeration* **31** (2008), 1123-1133.
- [25] C. Pang, J.W. Lee and Y.T. Kang, Review on combined heat and mass transfer characteristics in nanofluids, *International Journal of Thermal Sciences* **87** (2015), 49-67.
- [26] J. Sarkar, P. Ghosh and A. Adil, A review on hybrid nanofluids: recent research, development and applications, *Renewable and Sustainable Energy Reviews* **43** (2015), 164-177.
- [27] M. Lomascolo, G. Colangelo, M. Milanese and A.D. Risi, Review of heat transfer in nanofluids: conductive, convective and radiative experimental results, *Renewable and Sustainable Energy Reviews* **43** (2015), 1182-1198.
- [28] M. Ghanbarpour, E.B. Haghigi and R. Khodabandeh, Thermal properties and rheological behavior of water based Al<sub>2</sub>O<sub>3</sub> nanofluid as a heat transfer fluid, *Experimental Thermal and Fluid Science* **53** (2014), 227-235.
- [29] J. Albadr, S. Tayal and M. Alasadi, Heat transfer through heat exchanger using Al<sub>2</sub>O<sub>3</sub> nanofluid at different concentrations, *Case Studies in Thermal Engineering* **1** (2013), 38-44.

[30] A.S. Yadav and J.L. Bhagoria, Heat transfer and fluid flow analysis of solar air heater: A review of CFD approach, *Renewable and Sustainable Energy Reviews* **23** (2013), 60–79.

[31] Y. Wang, Y. He, W. Yang and Z. Cheng, Numerical analysis of flow resistance and heat transfer in a channel with delta winglets under laminar pulsating flow, *International Journal of Heat and Mass Transfer* **82** (2015), 51–65.

[32] J. Lacaze, S. Tierce, M.C. Lafont, Y. Thebault, N. Pebere, G. Mankowski, C. Blanc, H. Robidou, D. Vaumousse and D. Daloz, Study of the microstructure resulting from brazed aluminium materials used in heat exchangers, *Materials Science and Engineering A* **413–414** (2005), 317–321.

[33] A. Sharma, L.D. Won, D. Buddhi and J.U. Park, Numerical heat transfer studies of the fatty acids for different heat exchanger materials on the performance of a latent heat storage system, *Renewable Energy* **30** (2005), 2179–2187.

[34] F.P. Beer, E.R. Johnston Jr, J.T. Dewolf and D.F. Mazurek, *Mechanics of Materials*, 5th Edition, McGraw-Hill Press.

[35] M.A.K, Chowdhuri and Z. Xia, Interface bonding strength measurement of a joint between elastic and viscoelastic materials, *Composites: Part B* **44** (2013), 253–259.

[36] T. Kuvannarat, C. Wang and S. Wongwises, Effect of fin thickness on the air-side performance of wavy fin-and-tube heat exchangers under dehumidifying conditions, *International Journal of Heat and Mass Transfer* **49** (2006), 2587–2596.

[37] L. Chen, Z. Li and Z. Guo, Experimental investigation of plastic finned-tube heat exchangers, with emphasis on material thermal conductivity, *Experimental Thermal and Fluid Science* **33** (2009), 922–928.

[38] H. Yin and R. Ooka, Shape optimization of water-to-water plate-fin heat exchanger using computational fluid dynamics and genetic algorithm, *Applied Thermal Engineering* **80** (2015), 310-318.

[39] K. Guo, N. Zhang and R. Smith, Optimisation of fin selection and thermal design of counter-current plate-fin heat exchangers, *Applied Thermal Engineering* **78** (2015), 491-499.

[40] ANSYS Fluent 12.0, Theory guide, April 2009.

[41] ANSYS Mechanical APDL 15.0, Element reference, November 2013.

[42] R.G. Budynas, *Advanced Strength and Applied Stress Analysis*, 2<sup>nd</sup> Edition, McGraw-Hill Press, 1999.

[43] N. Tokgöz and M.M. Yavuz, Numerical investigation of heat transfer of nanofluid flow in a 3D channel with sharp edge rectangular ribs, *International Conference On Advances In Mechanical Engineering Istanbul, Turkey, 13-15 May 2015 - ICAME'15*, 385-392.